Non-Linear Modeling of a Vibro-Impact Wave Energy Converter

Bingyong Guo, *Member, IEEE*, and John V. Ringwood, *Senior Member, IEEE*

***Abstract*—This article proposes a non-linear vibro-impact mechanism, integrated inside a semi-submerged cylindrical buoy to form a self-contained and self-referenced vibro-impact wave energy converter (VIWEC), for performance enhancement. A non-linear mathematical model of the VIWEC is derived, considering linear wave-buoy interaction and non-linear vibro-impact mechanics. Numerical simulations are conducted to investigate the influence of the vibro-impact mechanism on the VIWEC's dynamics and performance. Numerical results conclude that the VIWEC is characterised by a band-pass frequency response and inherently decoupled from ocean waves of low frequencies, indicating high survivability under extreme sea states. The vibro-impact mechanism can also broaden the VIWEC's power capture bandwidth and limit the VIWEC's motion within its physical constraint. On the other hand, the VIWEC's dynamics are sensitive to design parameters, and an improper design may lead to rich and complex non-linear dynamics of the VIWEC, e.g. chaos and multi-stability. The proposed non-linear model can provide a platform for design optimisation and control development of the VIWEC.**

***Index Terms*—Non-linear modeling, non-linear dynamics, point absorber, vibro-impact mechanism, wave energy conversion.**

I. Introduction

COMPARED to solar and wind energy, wave energy is characterised by a high power density in space and a relatively continuous availability in time. For instance, the power intensities are 0.17 kW/m^2, 0.58 kW/m^2 and 8.42 kW/m^2 for solar, wind and wave energy at a latitude of 15°N within the North-East Trades, respectively [1]. However, wave energy is relatively untapped, due to the relatively high levelised cost of energy (LCoE) of wave energy for commercial applications. There are two main approaches to reduce the LCoE: (i) applying control or/and optimisation strategies to enhance the power conversion efficiency under moderate sea states and to improve system survivability under extreme sea states, and (ii) developing novel concepts of wave energy conversion systems or critical subsystems, e.g. power take-off (PTO) subsystems, which inherently have proprieties of a high power capture efficiency and a low requirement on maintenance.

Manuscript received December 4, 2019; revised April 10, 2020 and June 24, 2020; accepted July 3, 2020. Date of publication July 8, 2020; date of current version December 16, 2020. This work was supported in part by the European Union's Horizon 2020 research and innovation programme under the Marie Skłodowska-Curie grant agreement No 841388. Paper no. TSTE-01310-2019. *(Corresponding author: Bingyong Guo.)*

The authors are with the Centre for Ocean Energy Research, Maynooth University, Maynooth Co. Kildare, W23 F2K8, Ireland (e-mail: bingyong.guo@mu.ie; John.Ringwood@mu.ie).

Color versions of one or more of the figures in this article are available online at https://ieeexplore.ieee.org.

Digital Object Identifier 10.1109/TSTE.2020.3007926

Various technologies and devices for wave energy conversion have been examined [2]–[4], which can be classified into the following five predominant types: oscillating water columns, attenuators, point absorbers (PAs), terminators, and over-topping devices. Among the aforementioned wave energy converters (WECs), a heaving PA may be one of the simplest and most promising concepts [5], probably due to its favourable properties, e.g. easy to install, economical to operate. PAs can also be extended easily to form wave farms. Further, PAs can be categorised into three subtypes, including (i) single-body bottom-referenced PAs, e.g. the CETO buoy, (ii) two-body self-reacting PAs, e.g. the Wavebob buoy and OPT's PowerBuoy, and (iii) PA arrays, e.g. the WaveStar device.

The motion of PAs is large when resonance occurs, resulting in a high average power output. Unfortunately, PAs' resonance bandwidth is generally narrow, while wave spectra are wide-banded. In addition, wave spectra and frequencies vary from time to time, requiring manipulation of the device resonance frequency in real time. Consequently, control strategies have been developed and applied to maintain resonance conditions actively or passively [6], on the time scale of spectrum-to-spectrum or wave-to-wave. Alternatively, novel WEC and PTO concepts have been developed and tested to improve WECs' power absorption [7]–[10].

PTO systems are typically modelled as spring-damper systems, as shown in Fig. 1(a), reflecting the possibility to maximise power capture through complex conjugate control [6]. Non-linear mechanisms can be used to enhance the power capture performance of WECs [11]–[14]. For example, as shown in Fig. 1(b), two symmetrically oblique springs were used to achieve snap through mechanism, providing negative stiffness within a specific region of the heave motion [11]. Based on the same principle, a 'negative' spring, termed WaveSpring, was developed and tested by CorPower Ocean, and experimental data demonstrated that the power capture width was improved by a factor of 3 under normal operation mode [12]. In addition to non-linear springs, non-linear dampers were studied based on a self-contained mass-spring-damper PTO system [13], [14]. In Fig. 1(c), the damper can be a linear, mono-directional or quadratic damper. Both numerical and experimental data have shown that non-linear dampers tend to extract more energy than linear ones [13], [14].

The application of a vibro-impact mechanism in wave energy is inspired by its broad application in other engineering applications [15], e.g. vibro-impact moling machines, and impact drills. A very preliminary study on the use of vibro-impact

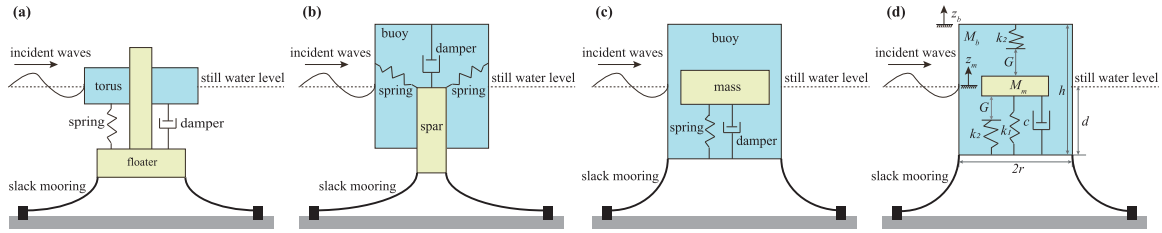

Fig. 1. Schematic diagrams of various two-body heaving point absorbers, with (a) a conventional spring-damper PTO system, (b) a bi-stable spring-damper PTO system, (c) a self-contained mass-spring-damper PTO system, and (d) a vibro-impact mass-spring-damper PTO system.

technology in wave energy is given in [16]. The current study aims to make use of the non-linearity of the vibro-impact mechanism to enhance the performance of a heaving PA, and the vibro-impact wave energy converter (VIWEC) is shown in Fig. 1(d). A floating buoy, with mass M_b, oscillates under the excitation of incident waves. An inner mass, M_m, is connected to the buoy by a supporting spring, with stiffness k_1, and a linear PTO damper, with coefficient c, and it oscillates due to the interaction force with the buoy. In practical application, a linear permanent magnet generator can be used as the PTO device, with its permanent magnets fixed to the buoy and coil winding acting as the movable inner mass. The key mechanism of the VIWEC is that the upper and lower impact springs, with stiffness k_2, attached to the top and floor of the buoy, provide impacts when the relative displacement between the buoy and the inner mass exceeds the upper or lower gap, G.

For heaving point absorbers, an end-stop function is required to limit the heave motion within physical constraints, especially when the wave height is large or resonance is achieved. End-stop springs were used to limit the heave motion when it exceeds a certain stroke threshold [17], [18] and the PAs' motion was changed significantly when the end-stop springs were active. In addition, the stroke threshold can significantly influence the response amplitude operator (RAO) and power capture of PAs [19]. The principle of the end-stop springs is the same as the vibro-impact mechanism in Fig. 1(d), and the occurrence of impact events can induce rich and complex non-linear dynamics, which is not addressed in the aforementioned studies but is addressed in this study. The proposed vibro-impact mechanism can limit the relative motion between the buoy and the inner mass within physical constraint when large impact gap and stiff impact springs are used. Alternatively, optimal control strategies can be applied to handle physical constraints for various PAs [20].

In this paper, a non-linear mathematical model of the VIWEC is derived, and numerical simulation is used to illustrate how the non-linear vibro-impact mechanism influences the VIWEC's dynamics and performance, in terms of RAO, average power, capture width ratio, and peak-to-average power ratio. Numerical results demonstrate that: i) The relative motion between the buoy and the inner mass has band-pass frequency characteristics, with a relative small RAO when the wave frequency is low. Hence, the VIWEC is inherently decoupled from waves and shows high survivability under extreme sea states, typified by low wave frequencies. ii) A properly designed vibro-impact mechanism can simultaneously broaden the bandwidth of VIWEC's RAO, enhance the average power, limit the relative motion within its physical constraint, and constrain the peak-to-average power ratio at a low level. iii) The VIWEC's non-linear dynamics and power absorption are sensitive to design parameters and wave conditions. Improper selection of design parameters may introduce complex and undesirable non-linear dynamics, e.g. chaos or/and multi-stability. Hence, novel optimisation and control strategies are required to match the VIWEC dynamics to a specific wave spectrum, to achieve power maximisation under moderate sea states, and to detune the device under extreme sea states.

The remainder of the paper is structured as follows. In Section II, a mathematical model of the VIWEC system is derived. Numerical simulations are conducted and discussed to investigate the impact-induced non-linear phenomena, bifurcations and multi-stability in Sections III–V, respectively. Conclusions are drawn in Section VI.

II. Modeling of Vibro-Impact Wave Energy Converter

The original motivation for this research was to investigate the feasibility of utilising WEC techniques for data buoys or smart buoys. Hence, the buoy dimension is close to the dimension of smart buoys, chosen as 2 m in diameter ($2r = 2$ m), 2 m in height ($h = 2$ m), and 1 m in draft ($d = 1$ m). The total mass of the buoy and the inner mass is set $M_b + M_m = 3220$ kg to ensure the buoy semi-submerged. The equations of motion of the VIWEC system are derived in this section, considering wave-buoy and buoy-mass interactions. The wave-buoy interaction is computed by solving a boundary value problem via NEMOH [21], resulting in an impulse response function (IRF) and a frequency response function (FRF) to represent the radiation and excitation forces, respectively. Since the non-parametric radiation IRF and excitation FRF are inconvenient for analysing the non-linear VIWEC dynamics, parametric state-space models with finite order are derived to approximate the radiation and excitation forces.

A. Equations of Motion

The dynamics of the buoy are governed by

$$M_b \ddot{z}_b = f_e + f_r + f_{hs} + f_i, \tag{1}$$

where f_e, f_r and f_{hs} represent the excitation, radiation and hydrostatic forces, respectively. f_i represents the interaction force between the buoy and the inner mass. z_b and $\ddot{z}_b$ are the heave

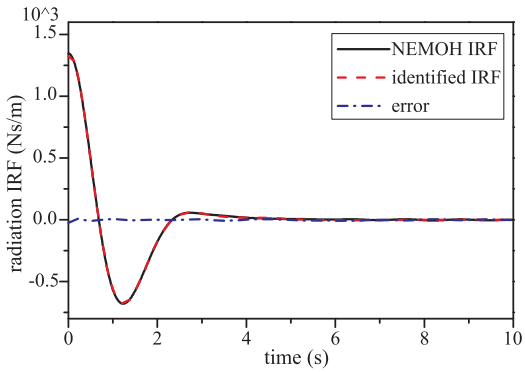

Fig. 2. Comparison of the radiation IRFs.

displacement and acceleration of the buoy, respectively. For simplicity, only heave motion is investigated, and the mooring force is omitted in this paper.

The motion of the inner mass is governed by

$$M_m \ddot{z}_m = -f_i, \tag{2}$$

where z_m and $\ddot{z}_m$ represent the displacement and acceleration of the inner mass, respectively. The interaction force f_i depends on the relative displacement between the inner mass and the buoy, including three cases as follows: i) when the relative displacement ($z_r = z_m - z_b$) is larger than or equal to the upper gap, $z_r \geq G$, the upper impact spring is active, and $f_i = k_1 z_r + k_2(z_r - G) + c v_r$, where $v_r = \dot{z}_r$ represents the relative velocity between the inner mass and the buoy; ii) when the relative displacement exceeds the lower gap, $z_r \leq -G$, the lower impact spring is active, and $f_i = k_1 z_r + k_2(z_r + G) + c v_r$; iii) when the relative displacement is within the two gaps, $G > z_r > -G$, only the supporting spring and the PTO damper are active, and $f_i = k_1 z_r + c v_r$. Therefore, f_i is summarised as

$$f_i = \begin{cases} k_1 z_r + k_2(z_r - G) + c v_r, & z_r \geq G; \\ k_1 z_r + c v_r, & G > z_r > -G; \\ k_1 z_r + k_2(z_r + G) + c v_r, & z_r \leq -G. \end{cases} \tag{3}$$

The hydrostatic force f_{hs} is given as

$$f_{hs} = -\rho g \pi r^2 z_b, \tag{4}$$

where $\rho = 1025\,\mathrm{kg/m^3}$ and $g = 9.81\,\mathrm{N/kg}$ are the water density and the gravity constant, respectively.

B. Radiation Force Approximation

The radiation force, in the time-domain, is given as

$$f_r = -m_\infty \ddot{z}_b - k_r * \dot{z}_b, \tag{5}$$

where $m_\infty = 1883\,\mathrm{kg}$ and $\dot{z}_b$ are the added mass at infinite frequency and the buoy velocity, respectively. k_r is the radiation IRF, shown in Fig. 2. The symbol $*$ represents the convolution operation, with the associated definition

$$f_{rc} = k_r * \dot{z}_b. \tag{6}$$

Finite order approximations of the radiation force were studied in the authors' earlier papers [22], [23], and hence a brief overview is given here. Realisation theory [24] and square-root balanced model reduction method [25] are applied on the radiation IRF to get a linear state-space model with finite order. The convolution term can be approximated by

$$\dot{x}_r = A_r x_r + B_r \dot{z}_b, \tag{7}$$

$$f_{rc} \approx C_r x_r, \tag{8}$$

where $x_r \in \mathbb{R}^{n\times 1}$ is the state vector. $A_r \in \mathbb{R}^{n\times n}$, $B_r \in \mathbb{R}^{n\times 1}$, $C_r \in \mathbb{R}^{1\times n}$ are the system matrices. n is the approximation order, selected by trial and error via evaluating the goodness of fit defined in [22]. In this study, $n = 4$ is used as its goodness of fit is 0.9998, with the system matrices given as

$$A_r = \begin{bmatrix} -1.50, -2.06, 1.54, -0.35 \\ 2.06, -0.01, 0.07, -0.02 \\ -1.54, 0.07, -2.38, 1.96 \\ -0.35, 0.02, -1.96, -0.54 \end{bmatrix}, \tag{9}$$

$$B_r = \begin{bmatrix} -403.88, 22.57, -181.05, -49.82 \end{bmatrix}', \tag{10}$$

$$C_r = \begin{bmatrix} -4.04, -0.23, 1.81, -0.50 \end{bmatrix}. \tag{11}$$

Alternatively, the radiation approximation problem can be solved in the frequency-domain [26]–[29], among which the moment-matching algorithm in [28], [29] can exactly match the frequency response of the original system at chosen frequencies and retain specific physical properties, e.g. passivity.

C. Excitation Force Approximation

The excitation force f_e can be determined quantitatively by its FRF, represented as

$$F_e(j\omega) = K_e(j\omega) A(j\omega), \tag{12}$$

where $K_e(j\omega)$ is the excitation FRF shown in Fig. 3(a), in terms of its amplitude response $|K_e(j\omega)|$ and phase response $\angle K_e(j\omega)$. $A(j\omega)$ is the frequency-domain representation of the incident wave $\eta(t)$, and ω is the wave frequency.

Alternatively, the excitation force can be expressed, in the time-domain, as

$$f_e(t) = k_e(t) * \eta(t) = \int_{-\infty}^{\infty} k_e(t-\tau)\eta(\tau) d\tau, \tag{13}$$

where $k_e(t)$ is the excitation IRF related to $K_e(j\omega)$, as

$$k_e(t) = \frac{1}{2\pi} \int_{-\infty}^{\infty} K_e(j\omega) e^{j\omega t} d\omega. \tag{14}$$

Based on the excitation FRF in Fig. 3(a), the excitation IRF $k_e(t)$ is represented by the black dash-dot curve in Fig. 3(b). Since $k_e(t) \neq 0$ for $t < 0$ (see the shadowed area in Fig. 3(b)), the wave-to-excitation-force process is non-causal.

Approximation approaches of the non-causal wave-to-excitation-force process were investigated numerically and experimentally in [30], [31], and a critical comparison of excitation force estimations is given in [32]. Hence, this paper only gives a brief overview of the excitation force approximation. According to the time shift property of the convolution operation, we have

$$f_e(t) = k_e(t) * \eta(t) = k_e(t - t_c) * \eta(t + t_c) = k_{e,c}(t) * \eta_p(t), \tag{15}$$

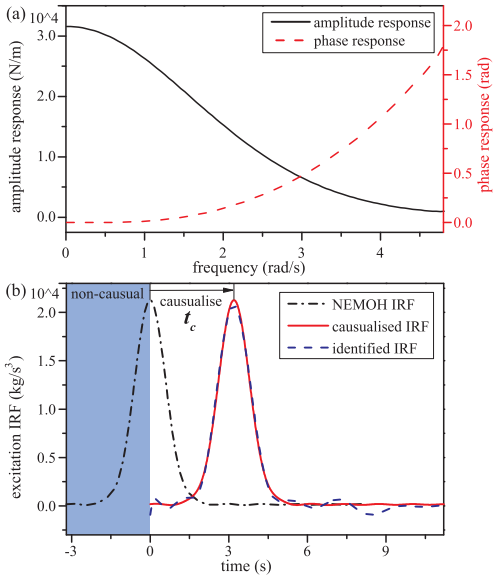

Fig. 3. (a) Excitation FRF represented by its amplitude response $|K_e(j\omega)|$ and phase response $\angle K_e(j\omega)$, and (b) non-causal, causualised and identified excitation IRFs.

where t_c ($t_c \geq 0$), $k_{e,c}(t) = k_e(t - t_c)$ and $\eta_p(t) = \eta(t + t_c)$ are the causalisation time, the causalised excitation IRF and the predicted wave elevation with t_c in advance, respectively. Hence, the causalised system, $k_{e,c}(t) * \eta_p(t)$, gives the same excitation force as the non-causal system, $k_e(t) * \eta(t)$.

Therefore, the excitation force can be approximated by

$$\dot{x}_e = A_e x_e + B_e \eta_p, \tag{16}$$

$$f_e \approx C_e x_e + D_e \eta_p, \tag{17}$$

where $x_e \in \mathbb{R}^{n\times 1}$ is the state vector. $A_e \in \mathbb{R}^{n\times n}$, $B_e \in \mathbb{R}^{n\times 1}$, $C_e \in \mathbb{R}^{1\times n}$ and $D_e \in \mathbb{R}^{1\times 1}$ are the system matrices. n is the approximation order. t_c and n are selected by trial and error by evaluating the truncation error and the goodness of fit defined in [31]. In this study, $t_c = 3.2\,\text{s}$ and $n = 6$ are used, and the identified excitation IRF is compared with its counterpart in Fig. 3(b), with a truncation error less than 0.0073 and a goodness of fit of 0.9953. The system matrices in Eqs. (16) and (17) are

$$A_e = \begin{bmatrix} -0.05, -0.61, -0.13, -0.24, -0.13, -0.12 \\ 0.61, -0.19, -1.13, -0.29, -0.39, -0.24 \\ -0.13, 1.13, -0.39, -1.56, -0.47, -0.52 \\ 0.24, -0.29, 1.56, -0.62, -2.04, -0.66 \\ -0.13, 0.39, -0.47, 2.04, -0.88, -2.38 \\ 0.12, -0.24, 0.52, -0.66, 2.38, -1.21 \end{bmatrix}, \tag{18}$$

$$B_e = \begin{bmatrix} -549.4, 884.3, -1008.7, 939.5, -784.6, 603.3 \end{bmatrix}', \tag{19}$$

$$C_e = \begin{bmatrix} -5.49, -8.84, -10.09, -9.39, -7.85, -6.03 \end{bmatrix}, \tag{20}$$

$$D_e = \begin{bmatrix} 49.85 \end{bmatrix}. \tag{21}$$

III. Impact-Induced Effect

To evaluate the VIWEC's dynamics and performance, the buoy, mass and relative RAOs are defined as

$$RAO_b = \frac{\max(z_b)}{H/2}, \tag{22}$$

$$RAO_m = \frac{\max(z_m)}{H/2}, \tag{23}$$

$$RAO_r = \frac{\max(z_r)}{H/2}, \tag{24}$$

where H represents the wave height. The instantaneous power, the average power and the peak-to-average power ratio are defined, respectively, as

$$P_i = c v_r^2, \tag{25}$$

$$P_a = \frac{1}{T}\int_0^T P_i \mathrm{d}t, \tag{26}$$

$$P_{p2a} = \frac{\max(P_i)}{P_a}, \tag{27}$$

where T is the wave period. The capture width ratio is defined

$$CWR = \frac{P_a}{2Jr}, \tag{28}$$

where $J = \frac{\rho g^2 T H^2}{32\pi}$ is the power density per wave crest per meter in width.

In this study, the harmonic wave is specified as $H = 0.8\,\text{m}$, $\omega \approx 2\,\text{rad/s}$ ($\omega \in (0.06, 4.8)\,\text{rad/s}$ for frequency-domain response), and its power flux is close to that of typical sea states in the Eastern Mediterranean and Aegean Seas [33]. For instance, the mean wave period at the measurement stations of Alanya, Dalaman and Bozcaada, varies from 2 to 6 s ($\omega \in (1, 3)\,\text{rad/s}$) [33]. This paper has a specific focus on the vibro-impact induced non-linear modelling and dynamics. Hence, irregular waves are not considered as the irregularity makes the dynamics even more complex. The device response can be evaluated deterministically in the time domain for irregular seas. However, given the dependence of any specific deterministic response to a polychromatic wave on a specific sea state realisation [34], summary statistics, which represent the response across a broad set of sea-state realisations, for these runs give a more realistic impression of actual performance. The vibro-impact parameters are selected as $M_m = 2000\,\text{kg}$ and $k_1 = 10000\,\text{N/m}$ to ensure the inner mass at the centre of the buoy, $c = 1100\,\text{Ns/m}$ close to the peak value of the radiation damping coefficient, $k_2 = 250000\,\text{N/m}$ and $G \in (0.04, 0.96)\,\text{m}$ to investigate the effectiveness of end-stop. At the critical point when the inner mass grazes the top or bottom of the buoy, the amplitude of the relative motion is $h/2$, indicating that $RAO_r = h/H$ is the physical constraint. In simulation, for-loop structure is used with zero initial condition for the first iteration. The last data set of current iteration is used as the initial condition for the following iteration. The simulation interval for each iteration is 300 wave periods, and the results of the last 20

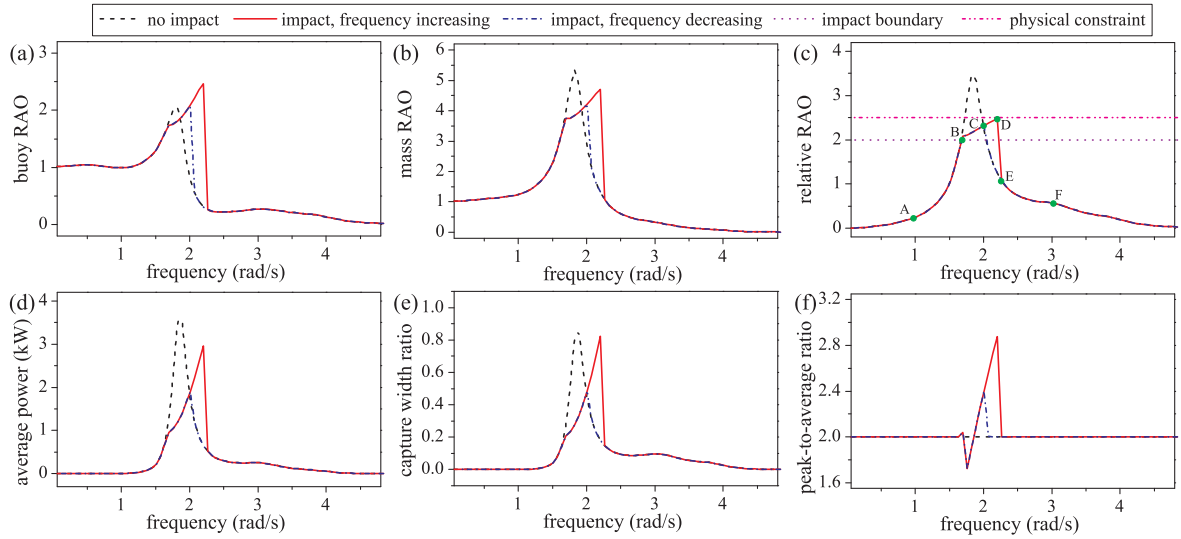

Fig. 4. (a) Buoy RAO, (b) mass RAO, (c) relative RAO, (d) average power, (e) capture width ratio, and (f) peak-to-average power ratio. Simulation conditions are $H = 0.8\,\text{m}$, $M_m = 2000\,\text{kg}$, $c = 1100\,\text{Ns/m}$, $G = 0.8\,\text{m}$, $k_1 = 10000\,\text{N/m}$, and $k_2 = 250000\,\text{N/m}$. For the case of no impact, $k_2 = 0\,\text{N/m}$ is used. The physical constraint is computed by h/H and the impact boundary is computed by $2\,G/H$.

wave periods are used to compute the performance indices in Eqs. (22)–(28).

The vibro-impact mechanism can influence the VIWEC's dynamics and performance significantly, which is illustrated in Fig. 4. As shown in Figs. 4(a)-(b), the buoy and mass RAOs have low-pass characteristics, while the relative RAO in Fig. 4(c) is more band-pass. When the wave frequency is low, the relative RAO is small and the average power is low, indicating that the VIWEC is inherently decoupled from the wave excitation force. Therefore, the system reliability is potentially high under extreme sea states, which consist of low wave frequencies. As shown in Fig. 4(a), the vibro-impact mechanism can enlarge the maximum value of the buoy RAO and widen its bandwidth, simultaneously. However, for the mass RAO in Fig. 4(b), its peak value is attenuated, but its bandwidth is broadened. Fig. 4(c) shows that the bandwidth of the relative RAO is widened and its peak value is limited within the physical constraint. The relative RAO can be reduced further, to ensure the end-stop function, by increasing the stiffness of the secondary springs or/and decreasing the impact gap (shown in Fig. 6(b)). Constrained optimal control [20] can also be used to prevent end-stop collision. Since the PTO performance only depends on the relative motion, the average power and the capture width ratio show the same trends as the relative RAO, with band-pass characteristics, widened bandwidth and attenuated peak value, which is shown in Figs. 4(d)-(e). The maximum average power is about $3\,\text{kW}$, and the maximum capture width ratio is about 0.8. As shown in Fig. 4(f), the peak-to-average power ratio is 2 when the vibro-impact mechanism is inactive ($k_2 = 0\,\text{N/m}$). When impacts occur, the peak-to-average power ratio can be either enlarged or attenuated. Its maximum value is around 2.8, enlarged by the vibro-impact mechanism.

On the negative side, the vibro-impact mechanism increases the system complexity of the VIWEC device, and introduces rich non-linear dynamics, e.g. jump and multi-stability phenomena. For instance, the relative RAO in Fig. 4(c) jumps from points D to E as the wave frequency increases. The relative RAO locus is $A \to B \to C \to D \to E \to F$ as the wave frequency increases, and $F \to E \to C \to B \to A$ as the wave frequency decreases. Therefore, multi-stability phenomena exist between the points C and E, within which the specific VIWEC dynamics depend heavily on initial conditions, discussed further in Section V.

Typical time traces are given in Fig. 5, with $\omega = 1\,\text{rad/s}$ in Fig. 5(a) to represent a relatively low wave frequency case, $\omega = 2.2\,\text{rad/s}$ in Figs. 5(b)-(c) to represent a resonance frequency case and to illustrate multi-stability phenomenon, and $\omega = 3\,\text{rad/s}$ in Fig. 5(d) to represent a relatively high wave frequency case. As shown in Fig. 5(a), the displacements of the buoy and the inner mass are in phase with each other, and the VIWEC acts as a 'wave follower', resulting in a small relative RAO. As a consequence, the instantaneous power and the average power are low. If desired, the bandwidth of the VIWEC can be extended into lower and/or higher frequencies using wave-by-wave control [6], which will also result in greater wetted surface variations. The average power is as low as $0.0053\,\text{kW}$, indicating that the VIWEC is fully decoupled from ocean waves typified by low frequencies. As shown in Fig. 5(b), no impact events occur. The buoy motion is small, but the mass motion is large. Hence, the relative RAO, the instantaneous power and the average power are greater than their counterparts in Fig. 5(a). As shown in Fig. 5(c), impact events occur, which amplifies the amplitudes of the buoy, mass and relative motions, leading to a much higher average power than its counterpart in Fig. 5(b). In Fig. 5(d), the motions of the buoy and the inner mass are small, but the relative motion is slightly larger than its counterpart in Fig. 5(a), since the displacements of the buoy and the inner mass are out of phase with each other.

Comparing Figs. 5(a), (b) and (d), the values of the relative RAO are 0.2464, 1.235 and 0.5654 for $\omega = 1\,\text{rad/s}$, $\omega =$

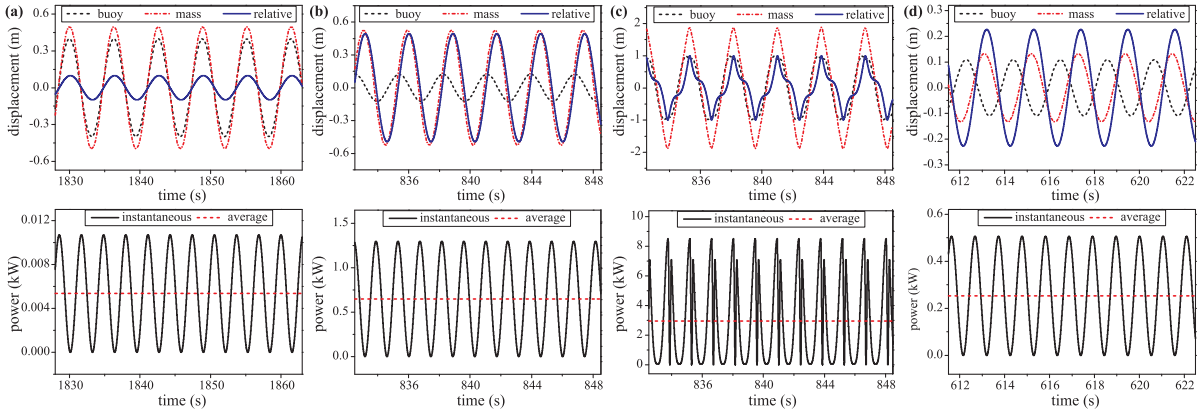

Fig. 5. Time traces of the buoy, mass and relative displacement, the instantaneous power, and the average power, with (a) $\omega = 1$ rad/s, (b)-(c) $\omega = 2.2$ rad/s, and (d) $\omega = 3$ rad/s. The other parameters are $H = 0.8$ m, $M_m = 2000$ kg, $c = 1100$ Ns/m, $G = 0.8$ m, $k_1 = 10000$ N/m, and $k_2 = 250000$ N/m. (b)-(c) illustrate the multi-stability phenomenon of the VIWEC system, with the initial conditions of $[z_{b0}, \dot{z}_{b0}, z_{m0}, \dot{z}_{m0}]' = [0, 0, 0, 0]'$ and $[z_{b0}, \dot{z}_{b0}, z_{m0}, \dot{z}_{m0}]' = [0, 0, 0, 3]'$, respectively.

2.2 rad/s and $\omega = 3$ rad/s, respectively. Therefore, the two-body VIWEC is a band-pass system, showing accordance to the results in Fig. 4(c). The average power is low when the frequency is relatively low, e.g. $P_a = 0.0053$ kW for $\omega = 1$ rad/s in Fig. 5(a), giving good immunity to potentially harmful and high-energy sea states. The average power is high when the wave frequency is close to the resonance frequency, e.g. $P_a = 0.6496$ kW for $\omega = 2.2$ rad/s in Fig. 5(b). The average power is low when the frequency is relatively high, e.g. $P_a = 0.2531$ kW for $\omega = 3$ rad/s in Fig. 5(d), consistent with the band-pass characteristic as shown in Fig. 4. Comparing Figs. 5(b)-(c), multi-stability is manifest. The average power is amplified by a factor of 4.56 by impact events, from $P_a = 0.6496$ kW to $P_a = 2.9612$ kW, while the peak-to-average power ratio only increases from 2 to 2.8, by a factor of 1.4. On the other hand, the VIWEC's dynamics are sensitive to initial conditions due to the existence of multi-stability, further discussed in Section V.

IV. Impact-Induced Bifurcation

The non-linear dynamics of the VIWEC are sensitive to the design parameters, including M_m, k_1, k_2, G and c, and the wave conditions, in terms of wave height H and period T. Among these parameters, G is one of the most critical parameters which can directly influence the occurrence of impact events and induce rich and complex non-linear dynamics of the VIWEC. In this section, the impact gap G is taken as an example to conduct bifurcation analysis, to illustrate how the design parameters influence the non-linear dynamics of the VIWEC system, with the results shown in Fig. 6. In Fig. 6, the red dots in the phase portraits are the Poincaré section points, defined as

$$z_r^* = z_r(nT), \tag{29}$$

$$v_r^* = v_r(nT), \tag{30}$$

where $n = 1, 2, 3, \cdots$ is the period number of the wave.

In Fig. 6, the gap is varied over a broad range, as $G \in [0.04, 0.96]$ m. In Fig. 6(a), v_r^* loci are represented by black and green dots as the gap increases, and by red dots as the gap decreases. According to the variation in the VIWEC's dynamics, the range $G \in [0.04, 0.96]$ m can be divided into 8 zones. The VIWEC's dynamics in each zone are detailed as follows:

- In zones 1, 3, 6 and 8, only one stable orbit exists, and the VIWEC's dynamics are periodic. A typical example of $G = 0.5$ m is shown in Fig. 6(i), with the time traces of the buoy, mass and relative displacements, the instantaneous power and the average power, and the phase portrait of the relative motion. During one wave period, one upper and one lower impact events occur. The gap value in zone 6 is preferred, as the relative motion in Fig. 6(b) is effectively limited within the physical constraint, the average power in Fig. 6(c) is higher, varying from 1 kW to 2 kW, and the peak-to-average power ratio in Fig. 6(d) varies from 3 to 4.
- In zones 2 and 4, the system dynamics are chaotic. Consequently, the peak-to-average power ratio in Fig. 6(d) varies significantly. Fig. 6(e) illustrates typical time traces and phase portrait for $G = 0.15$ m. There is no obvious period in the buoy, mass and relative displacements, and the instantaneous power appears to be 'irregular,' even though the incident wave is harmonic. In application, the gap value in these zones should be avoided since the complex dynamics induce a large total harmonic distortion to the captured power.
- In zones 5 and 7, multi-stability phenomena exist. For instance, there are 3 possible orbits for $G = 0.23$ m, illustrating the tri-stability of the VIWEC's dynamics. As shown in Figs. 6(f)-(g), the period of the orbits is twice the wave period, while its counterpart in Fig. 6(h) is identical to the wave period. Figs. 6(f)-(h) also illustrate that each specific instance of the VIWEC's dynamics depends heavily on initial conditions. Compared to the value in zone 5, the gap value in zone 7 is preferred as there are only two possible orbits, of which the black and red dots represent the orbits with and without impacts, respectively. As shown in Fig. 6(c), the black one with impacts can generate higher power than the red one without impacts. However, the attraction of the orbits depends heavily on initial conditions. Therefore, extra effort is required to ensure the attraction of the orbit represented by black dot for higher

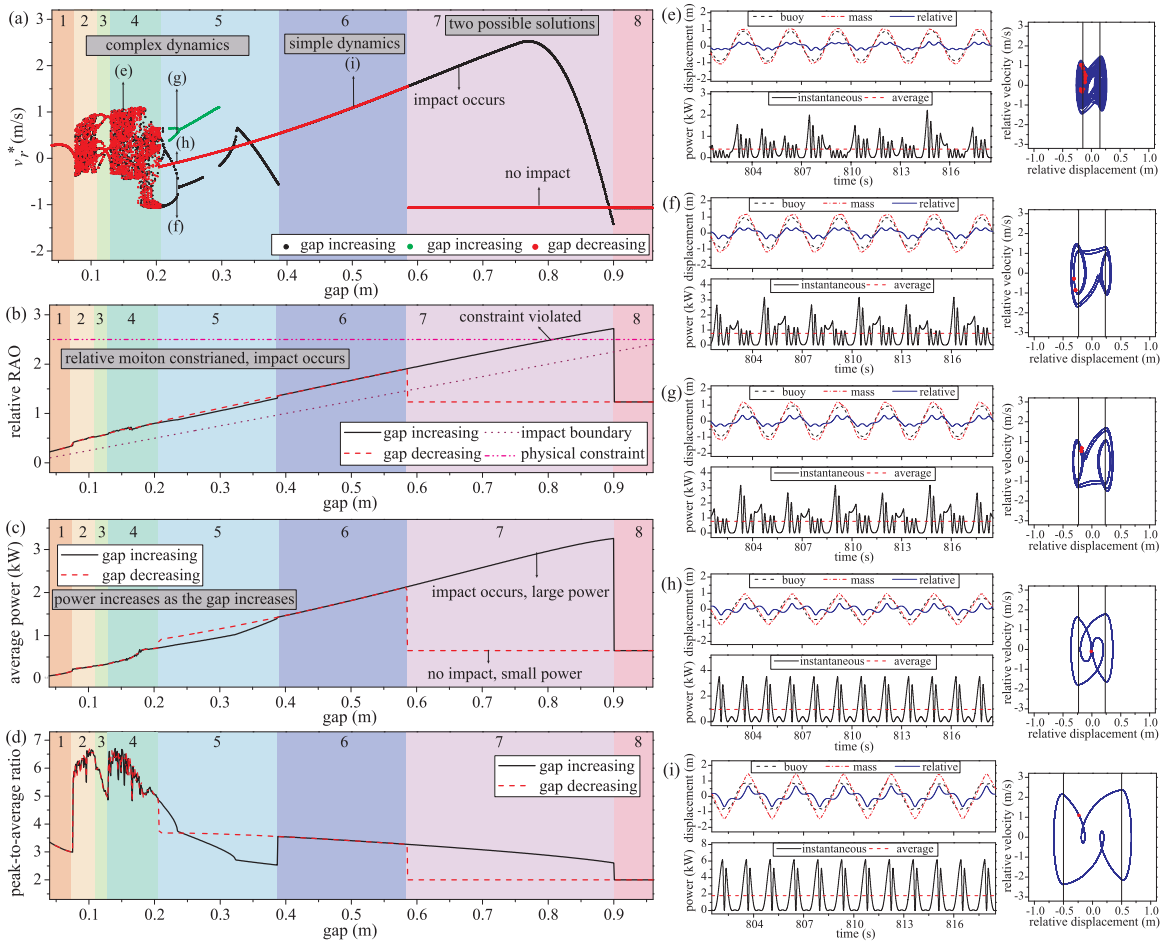

Fig. 6. (a) Bifurcation diagram of Poincaré section points, (b) relative RAO, (c) average power and (d) peak-to-average power ratio by varying the gap values, $G \in [0.04, 0.96]$ m, and (e)-(i) typical time traces and phase portraits. The gap values are $G = 0.15$ m for (e), $G = 0.23$ m for (f)-(h), and $G = 0.50$ m for (i). The other parameters are $H = 0.8$ m, $\omega = 2.2$ rad/s, $M_m = 2000$ kg, $c = 1100$ Ns/m, $k_1 = 10000$ N/m, and $k_2 = 250000$ N/m. (f)-(h) illustrate multi-stability of the VIWEC system, with initial conditions of $[z_{b0}, \dot{z}_{b0}, z_{m0}, \dot{z}_{m0}]' = [0, 0, -0.3467, 0.6]'$, $[z_{b0}, \dot{z}_{b0}, z_{m0}, \dot{z}_{m0}]' = [-0.6, 0, 0, 0]'$ and $[z_{b0}, \dot{z}_{b0}, z_{m0}, \dot{z}_{m0}]' = [0, 0, 0, 0]'$, respectively. In the phase portraits, the black vertical lines are the upper and lower impact boundaries ($\pm G$), and the red dots are the Poincaré section points defined in Eqs. (29)–(30).

power capture. In Fig. 6(b), the relative motion violates the physical constraint for $G \in (0.81, 0.91)$ m. These values should be avoided for effective end-stop protection.

Grazing and period-halving bifurcations are observed in Fig. 6(a). For instance, grazing bifurcations occur around $G = 0.075$ m and $G = 0.129$ m, resulting in chaotic motion from periodic motion, and around $G = 0.107$ m, leading to periodic motion from chaotic motion. A period-halving bifurcation occurs around $G = 0.205$ m, leading to periodic motion from chaotic motion. Comparing Figs. 6(a)-(d), it is clear that the system performance, in terms of relative RAO, average power and peak-to-average power ratio, is sensitive to the variation in G.

As the gap increases from 0.1 m to 0.9 m, the relative RAO and the average power increase, while the peak-to-average power ratio decreases. However, the gap is bounded by the buoy height ($G < h/2$) and the physical constraint ($RAO_r < h/H$). In addition, a bifurcation analysis in Fig. 6 provides basic guidelines for prototyping the VIWEC. The gap value in zone 6, to say $G \in (0.39, 0.59)$ m, is appropriate, as the VIWEC's dynamics are simple, the relative RAO is limited within the physical constraint, the average power is higher than 1 kW, and the peak-to-average power ratio is less than 3.5. Some gap values in zone 7, to say $G \in (0.59, 0.81)$ m, is preferred only if the orbit with impact events is ensured by extra efforts, i.e. control of multi-stability [35], [36]. In addition, similar non-linear dynamics of the VIWEC can be observed by varying other parameters, and G is taken as a typical example in this study.

V. Impact-Induced Multi-Stability

As discussed in Sections IV and V, the vibro-impact mechanism increases the system complexity, and may induce multi-stability phenomena. When multi-stability exists for a certain set of design parameters, the specific VIWEC's dynamics depend heavily on initial conditions. A basin of attraction is used here to identify a set of initial conditions leading to the same long-term behaviour of the VIWEC system. Such long-term VIWEC's behaviour may be considered to be an attractor, and

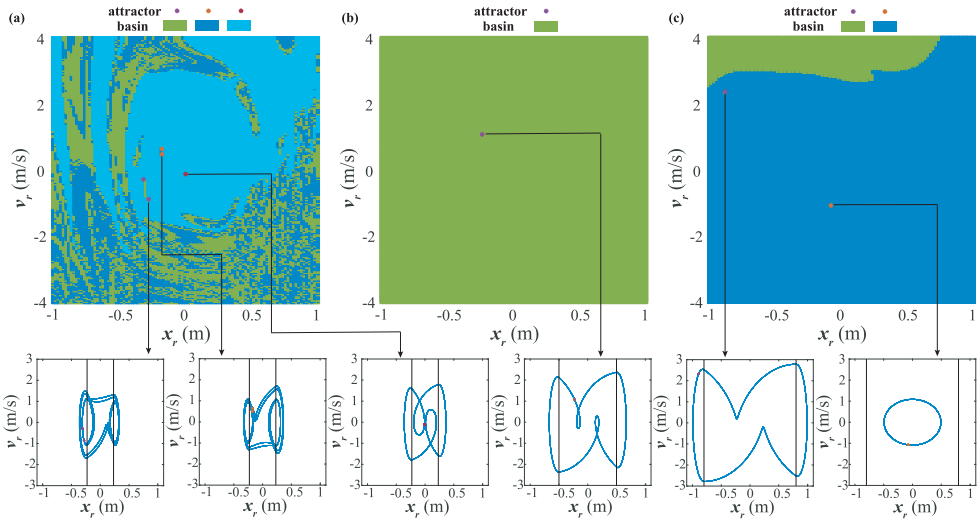

Fig. 7. Basin diagrams for (a) $G = 0.23$ m, (b) $G = 0.5$ m, and (c) $G = 0.8$ m, with the phase portrait for each attractor. The simulation conditions are $H = 0.8$ m, $\omega = 2.2$ rad/s, $M_m = 2000$ kg, $c = 1100$ Ns/m, $k_1 = 10000$ N/m, and $k_2 = 250000$ N/m. In the phase portraits, the black vertical lines are the upper and lower impact boundaries ($\pm G$), and the dots are the Poincaré section points defined in Eqs. (29)–(30).

the corresponding set of associated initial conditions forms the basin of attraction. For $G = 0.23$ m, $G = 0.5$ m and $G = 0.8$ m, their basin diagrams are shown in Figs. 7(a)-(c), in which the dots represent the attractors and the painted areas represent the basins of attraction.

In Fig. 7(a), there exist three attractors, with the first, second and third attractors marked by purple, orange, and maroon dots, and their basins are painted in green, blue and sky blue, respectively. Notably, the basins of the first and second attractors overlap with each other. However, their orbits are symmetric with respect to the origin, leading to the same system performance, in terms of relative RAO, average power and peak-to-average power ratio. The time traces of the three attractors are shown in Figs. 6(f)-(h). In Fig. 7(b), there only exists one stable orbit within the area of interest, and the VIWEC's dynamics are simple, with indicative time traces shown in Fig. 6(i). In Fig. 7(c), two orbits coexist. For the first attractor, one upper and one lower impact events occur during one wave period, and no impact occurs for the second attractor. The first orbit occupies a larger relative motion envelop than the second one, resulting in much higher average power. However, the area of the basin of the first attractor is much smaller than that of the second one. The time traces of the two attractors are shown in Figs. 5(b)-(c), emphasising that the vibro-impact mechanism can extend the VIWEC's relative RAO and average power. When multiple orbits coexist, control of multi-stability can be used to switch the system dynamics from one attractor to another [35], [36], which indicates the possibility of tuning and detuning the system dynamics.

VI. Conclusion

In this study, a non-linear mathematical model for the VIWEC system is derived, based on linear wave-buoy interaction and a non-linear vibro-impact mechanism. For the wave-buoy interaction, the radiation and excitation forces are approximated by finite-order linear systems. Numerical simulation is used to investigate the non-linear dynamics of the VIWEC device. The VIWEC's dynamics have band-pass characteristics, with small relative motion for a low wave frequency. As extreme sea states typically consist of low wave frequencies, the VIWEC device is inherently decoupled from extreme waves, resulting in small relative motion and low average power. Therefore, the vibro-impact mechanism can be used to improve system survivability under extreme sea states. The results presented also show the performance of an essentially uncontrolled system, which has the appealing characteristic of spilling power in high-energy (low frequency), potentially destructive, sea states. If desired, the high-frequency (low-energy) power capture characteristics of the device can be enhanced using real-time control. The vibro-impact mechanism uses stiff upper and lower impact springs, simultaneously providing effective end-stop function to limit the VIWEC's relative motion, and broadening the power capture bandwidth. However, the resonance frequency and peak-to-average power ratio may increase slightly due to the occurrence of impact events.

Numerical results also show that the VIWEC's dynamics are sensitive to the design parameters of the vibro-impact mechanism. The bifurcation analysis, using the gap G as a parameter, illustrates that the VIWEC's dynamics experience grazing and period-halving bifurcations, chaotic and periodic motions, and coexistence of multi-stability. The VIWEC's performance, in terms of average power and peak-to-average power ratio, varies correspondingly. It is possible to achieve end-stop avoidance, bandwidth widening and power enhancement, simultaneously, by parametric study and design optimisation to fit the VIWEC frequency response to a specific wave spectrum. However, such design optimisation is very challenging to conduct as it is subjected to multi-parameter and multi-criterion. When multiple orbits coexist, the VIWEC's dynamics depend heavily on initial conditions. Some orbits indicate higher average power, while others indicate lower average power. This property provides a

possibility to tune or detune the VIWEC's dynamics and performance by control of multi-stability, in switching between orbits.

On-going work focuses on parametric analysis of the VIWEC system to investigate how the design parameters influence the VIWEC's dynamics and performance, which will provide basic guidelines for prototyping and wave tank testing.

Acknowledgment

This paper reflects only the authors' view and that the Agency is not responsible for any use that may be made of the information it contains.

References

[1] M. E. McCormick, *Ocean Wave Energy Conversion*. New York, NY, USA: Wiley, 1981.
[2] B. Drew, A. Plummer, and M. N. Sahinkaya, "A review of wave energy converter technology," *P. I. Mech. Eng. A-J. Pow.*, vol. 223, no. 8, pp. 887–902, 2009.
[3] A. Babarit, J. Hals, M. Muliawan, A. Kurniawan, T. Moan, and J. Krokstad, "Numerical benchmarking study of a selection of wave energy converters," *Renew. Energ.*, vol. 41, pp. 44–63, 2012.
[4] A. F. d. O. Falcão, "Wave energy utilization: A review of the technologies," *Renew. Sust. Energ. Rev.*, vol. 14, no. 3, pp. 899–918, 2010.
[5] P. Ricci, J. Lopez, M. Santos, J. Villate, P. Ruiz-Minguela, F. Salcedo, and A. D. O. Falcão, "Control strategies for a simple point-absorber connected to a hydraulic power take-off," in *Proc. EWTEC*, Uppsala, Sweden, 2009.
[6] J. V. Ringwood, G. Bacelli, and F. Fusco, "Energy-maximizing control of wave-energy converters: The development of control system technology to optimize their operation," *IEEE Control Syst. Mag.*, vol. 34, no. 5, pp. 30–55, 2014.
[7] Y. Wei, J. Barradas-Berglind, M. van Rooij, W. Prins, B. Jayawardhana, and A. Vakis, "Investigating the adaptability of the multi-pump multi-piston power take-off system for a novel wave energy converter," *Renew. Energ.*, vol. 111, pp. 598–610, 2017.
[8] B. Kim, J. Wata, M. A. Zullah, M. R. Ahmed, and Y. Lee, "Numerical and experimental studies on the PTO system of a novel floating wave energy converter," *Renew. Energ.*, vol. 79, pp. 111–121, 2015.
[9] G. Bracco, A. Cagninei, E. Giorcelli, G. Mattiazzo, D. Poggi, and M. Raffero, "Experimental validation of the ISWEC wave to PTO model," *Ocean Eng.*, vol. 120, pp. 40–51, 2016.
[10] L. Papillon, L. Wang, N. Tom, J. Weber, and J. V. Ringwood, "Parametric modelling of a reconfigurable wave energy device," *Ocean Eng.*, 2019, doi: 10.1016/j.oceaneng.2019.06.010.
[11] X. Zhang and J. Yang, "Power capture performance of an oscillating-body wec with nonlinear snap through PTO systems in irregular waves," *Appl. Ocean Res.*, vol. 52, pp. 261–273, 2015.
[12] J. H. Todalshaug *et al.*, "Tank testing of an inherently phase-controlled wave energy converter," *Int. J. Mar. Energy*, vol. 15, pp. 68–84, 2016.
[13] H. Bailey and I. G. Bryden, "Influence of a quadratic power take-off on the behaviour of a self-contained inertial referenced wave energy converter," *P. I. Mech. Eng. M-J. Eng.*, vol. 226, no. 1, pp. 15–22, 2012.
[14] H. Bailey, "The effect of a nonlinear power take off on a wave energy converter," Ph.D. dissertation, The Univ. Edinburgh, 2009.
[15] R. A. Ibrahim, *Vibro-Impact Dynamics: Modeling, Mapping and Applications*. Berlin, Germany: Springer Science & Business Media, 2009.
[16] B. Guo and J. V. Ringwood, "Modelling of a vibro-impact power take-off mechanism for wave energy systems," in *Proc. ECC*, Saint Petersburg, Russia, 2020, pp. 1348–1353.
[17] W. Chen, I. Dolguntseva, A. Savin, Y. Zhang, W. Li, O. Svensson, and M. Leijon, "Numerical modelling of a point-absorbing wave energy converter in irregular and extreme waves," *Appl. Ocean. Res.*, vol. 63, pp. 90–105, 2017.
[18] M. Göteman *et al.*, "Wave loads on a point-absorbing wave energy device in extreme waves," in *Proc. ISOPE*, HI, USA, 2015.
[19] M. Jaya Muliawan, Z. Gao, T. Moan, and A. Babarit, "Analysis of a two-body floating wave energy converter with particular focus on the effects of power take-off and mooring systems on energy capture," *J. Offshore Mech. Arct.*, vol. 135, no. 3, 2013.
[20] G. Bacelli and J. V. Ringwood, "Numerical optimal control of wave energy converters," *IEEE T. Sustain. Energ.*, vol. 6, no. 2, pp. 294–302, Apr. 2015.
[21] A. Babarit and G. Delhommeau, "Theoretical and numerical aspects of the open source BEM solver NEMOH," in *Proc. EWTEC*, Nantes, France, 2015.
[22] B. Guo, R. Patton, S. Jin, J. Gilbert, and D. Parsons, "Nonlinear modeling and verification of a heaving point absorber for wave energy conversion," *IEEE T. Sustain. Energ.*, vol. 9, no. 1, pp. 453–461, 2017.
[23] A. Roessling and J. V. Ringwood, "Finite order approximations to radiation forces for wave energy applications," *Renew. Energies Offshore*, pp. 359–366, 2015.
[24] S. Kung, "A new identification and model reduction algorithm via singular value decomposition," in *Proc. 12th Asilomar Conf. Circuits, Syst. Comput.*, CA, USA, 1978, pp. 705–714.
[25] M. Safonov and R. Chiang, "A schur method for balanced model reduction," in *Proc. ACC*, Atlanta, GA, USA, 1988, pp. 1036–1040.
[26] R. Taghipour, T. Perez, and T. Moan, "Hybrid frequency–time domain models for dynamic response analysis of marine structures," *Ocean Eng.*, vol. 35, no. 7, pp. 685–705, 2008.
[27] T. Perez and T. I. Fossen, "A MATLAB toolbox for parametric identification of radiation-force models of ships and offshore structures," *Model Identif. Control.*, vol. 30, no. 1, pp. 1–15, 2009.
[28] N. Faedo, Y. Peña-Sanchez, and J. V. Ringwood, "Finite-order hydrodynamic model determination for wave energy applications using moment-matching," *Ocean. Eng.*, vol. 163, pp. 251–263, 2018.
[29] Y. Peña-Sanchez *et al.*, "Finite-order hydrodynamic approximation by moment-matching (FOAMM) toolbox for wave energy applications," in *Proc. EWTEC*, Naples, Italy, 2019.
[30] B. Guo, R. Patton, and S. Jin, "Identification and validation of excitation force for a heaving point absorber wave energy convertor," in *Proc. EWTEC*, Cork, Ireland, 2017.
[31] B. Guo, R. J. Patton, S. Jin, and J. Lan, "Numerical and experimental studies of excitation force approximation for wave energy conversion," *Renew. Energ.*, vol. 125, pp. 877–889, 2018.
[32] Y. Peña-Sanchez, C. Windt, J. Davidson, and J. V. Ringwood, "A critical comparison of excitation force estimators for wave-energy devices," *IEEE Trans. Control Syst. Technol.*, 2019, doi: 10.1109/TCST.2019.2939092.
[33] B. Ayat, "Wave power atlas of Eastern Mediterranean and Aegean Seas," *Energy.*, vol. 54, pp. 251–262, 2013.
[34] A. Mérigaud and J. V. Ringwood, "Free-surface time-series generation for wave energy applications," *IEEE J. Ocean. Eng.*, vol. 43, no. 1, pp. 19–35, 2017.
[35] A. N. Pisarchik and U. Feudel, "Control of multistability," *Phys. Rep.*, vol. 540, no. 4, pp. 167–218, 2014.
[36] Y. Liu, M. Wiercigroch, J. Ing, and E. Pavlovskaia, "Intermittent control of coexisting attractors," *Phil. Trans. R. Soc. A*, vol. 371, no. 1993, pp. 1–15, 2013.

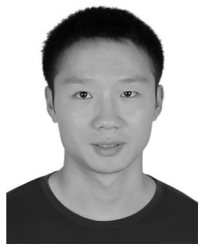

Bingyong Guo (Member, IEEE) received the B.Eng. and M.Sc. degrees in information countermeasure technology and underwater acoustics, from Nortwestern Polytechnical University in 2010 and 2013, respectively. He received the Ph.D. degree in Electronic Engineering at the University of Hull in 2017. He is currently a Postdoctoral researcher at the Centre for Ocean Energy Research, Maynooth Univerity. His current research interests are in the numerical modeling, experimental verification and optimal control system design of wave energy conversion devices.

John V. Ringwood (Senior Member, IEEE) received the Diploma degree in electrical engineering from the Dublin Institute of Technology, Dublin, Ireland, and the Ph.D. degree in control systems from University of Strathclyde, Glasgow, U.K., in 1981 and 1985, respectively. He is currently Professor of Electronic Engineering with Maynooth University, Ireland, where he is also the Director of the Centre for Ocean Energy Research. His current research interests include time series modeling, wave energy and biomedical engineering. Dr. Ringwood is also a Chartered Engineer and a Fellow of Engineers Ireland.